



Superconductivity in a quintuple-layer square-planar nickelate

Grace A. Pan¹, Dan Ferenc Segedin¹, Harrison LaBollita², Qi Song¹, Emilian M. Nica², Berit H. Goodge^{3,4}, Andrew T. Pierce¹, Spencer Doyle¹, Steve Novakov⁵, Denisse Córdova Carrizales¹, Alpha T. N'Diaye⁶, Padraic Shafer⁶, Hanjong Paik⁷, John T. Heron⁸, Jarad A. Mason⁹, Amir Yacoby¹, Lena F. Kourkoutis^{3,4}, Onur Erten², Charles M. Brooks¹, Antia S. Botana²✉ and Julia A. Mundy¹✉

Since the discovery of high-temperature superconductivity in copper oxide materials¹, there have been sustained efforts to both understand the origins of this phase and discover new cuprate-like superconducting materials². One prime materials platform has been the rare-earth nickelates and, indeed, superconductivity was recently discovered in the doped compound Nd_{0.8}Sr_{0.2}NiO₂ (ref. ³). Undoped NdNiO₂ belongs to a series of layered square-planar nickelates with chemical formula Nd_{n+1}Ni_nO_{2n+2} and is known as the ‘infinite-layer’ ($n = \infty$) nickelate. Here we report the synthesis of the quintuple-layer ($n = 5$) member of this series, Nd₆Ni₅O₁₂, in which optimal cuprate-like electron filling ($d^{8.8}$) is achieved without chemical doping. We observe a superconducting transition beginning at ~13 K. Electronic structure calculations, in tandem with magnetoresistive and spectroscopic measurements, suggest that Nd₆Ni₅O₁₂ interpolates between cuprate-like and infinite-layer nickelate-like behaviour. In engineering a distinct superconducting nickelate, we identify the square-planar nickelates as a new family of superconductors that can be tuned via both doping and dimensionality.

Attempts to construct materials that are isoelectronic and isostructural to the cuprates as candidate superconducting systems have spanned more than three decades². In this context, nickelate materials have been of enduring interest due to the proximity of nickel and copper in the periodic table⁴; furthermore, Ni¹⁺ has the same d^9 electron count as Cu²⁺. With continued understanding of the hallmarks of cuprate superconductivity—including, for example, a prominent orbital polarization, strong transition metal–oxygen hybridization or a quasi-two-dimensional square lattice—general attention to nickelates has been refined to specific proposals for LaNiO₃/LaMO₃ superlattices (M, trivalent cation)⁵ and La_{2-x}Sr_xNiO₄ (ref. ⁶). To date, superconductivity has not been realized in any of these originally proposed materials. Most recently, however, Sr-doped NdNiO₂, the so-called ‘infinite-layer’ nickelate, has been shown to be superconducting³, with a dome-like doping dependence for the superconducting transition temperature, T_c , centred around $d^{8.8}$ nickel filling^{7,8}.

Following this observation of superconductivity in Sr-doped NdNiO₂, there has been considerable interest in determining how ‘cuprate-like’ these infinite-layer nickelates are. For example, while the cuprates are often described by a single-band Hubbard model, electronic structure descriptions of the infinite-layer nickelates invoke multiband models, including hybridisation with the rare-earth $5d$ bands^{9–11}. Infinite-layer nickelates also seem to exhibit a much larger charge-transfer energy than their cuprate counterparts^{10–12}. Experimentally, the synthesis of these compounds remains challenging¹³ and to date there are only three independent reports of superconductivity^{3,8,14}, all in the chemically doped infinite-layer compound. These extended difficulties in reproducing nickelate superconductivity have generated a flurry of questions involving the synthetic challenges, the substrate–film interface^{15,16} and, most importantly, whether there exists an entire family of nickelate superconductors beyond compounds accessible through isovalent cation substitution.

Here, we note that NdNiO₂ is the end, or ‘infinite’ ($n = \infty$), member compound of the broader layered R_{n+1}Ni_nO_{2n+2} (R, trivalent rare-earth cation, $n > 1$) series. This family of layered materials possesses quasi-two-dimensional NiO₂ planes in a square-planar coordination with rare-earth fluorite blocking slabs interleaved every n nickel layers. These square-planar compounds are obtained via oxygen deintercalation from the corresponding parent perovskite RNiO₃ ($n = \infty$) and Ruddlesden–Popper R_{n+1}Ni_nO_{3n+1} ($n \neq \infty$) phases (Fig. 1b). As shown in Fig. 1a, the R_{n+1}Ni_nO_{2n+2} series can be mapped onto the cuprate phase diagram in terms of the nickel $3d$ electron count using formal valence-counting rules (Supplementary Note 1), where the end member NdNiO₂ has d^9 (Ni¹⁺) filling. The trilayer R₄Ni₃O₈ ($n = 3$, R = La or Pr) nickelates have been reported as close cuprate analogues, although superconductivity has not been observed¹⁷. Both La₄Ni₃O₈ and Pr₄Ni₃O₈ exhibit strong orbital polarization¹⁷ with a large cuprate-like magnetic superexchange¹⁸, strengthening the connection to the cuprate phase diagram. These trilayer nickelates have an average $d^{8.67}$ (Ni^{1.33+}) filling across the nickel planes (note that in multilayer cuprates, NMR experiments have shown that there is a layer-resolved doping profile¹⁹), lying in the ‘overdoped’ regime of the cuprate phase diagram. Meanwhile,

¹Department of Physics, Harvard University, Cambridge, MA, USA. ²Department of Physics, Arizona State University, Tempe, AZ, USA. ³School of Applied and Engineering Physics, Cornell University, Ithaca, NY, USA. ⁴Kavli Institute at Cornell for Nanoscale Science, Cornell University, Ithaca, NY, USA.

⁵Department of Physics, University of Michigan, Ann Arbor, MI, USA. ⁶Advanced Light Source, Lawrence Berkeley National Laboratory, Berkeley, CA, USA.

⁷Platform for the Accelerated Realization, Analysis, and Discovery of Interface Materials (PARADIM), Cornell University, Ithaca, NY, USA. ⁸Department of Materials Science and Engineering, University of Michigan, Ann Arbor, MI, USA. ⁹Department of Chemistry and Chemical Biology, Harvard University, Cambridge, MA, USA. ✉e-mail: antia.botana@asu.edu; mundy@fas.harvard.edu

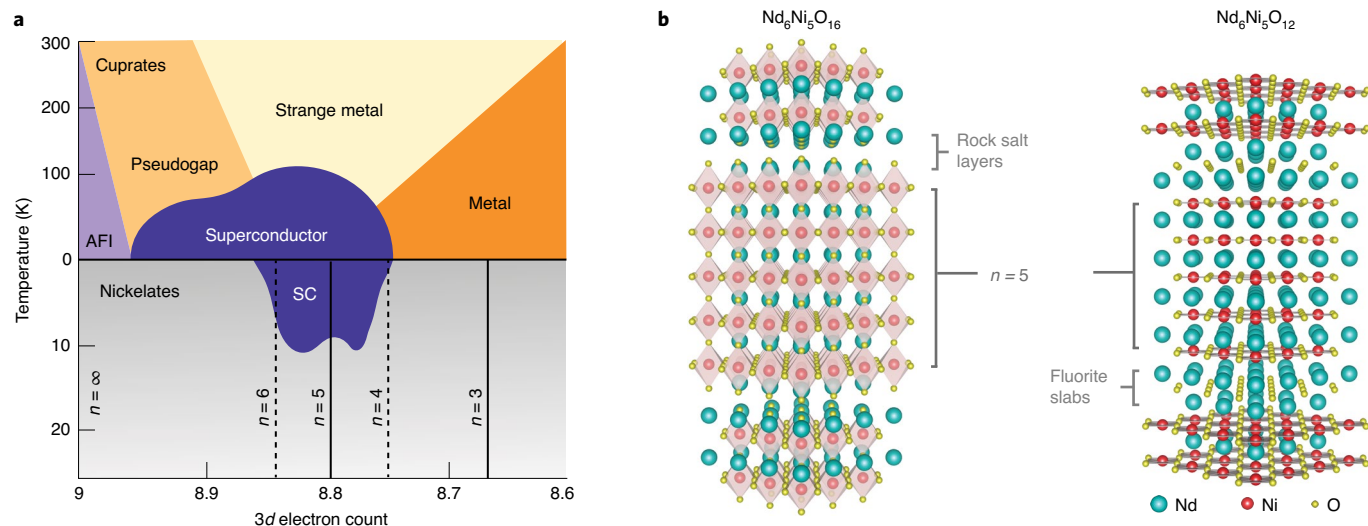


Fig. 1 | Electronic phase diagram and structural description of the layered nickelates. **a**, Schematic phase diagram for the electronic phases of the cuprates (top) and nickelates (bottom). The superconducting dome for the cuprates is adapted from ref. ²; for the nickelates, from Sr-doped NdNiO_2 (refs. ^{7,8}). The square-planar $\text{R}_{n+1}\text{Ni}_n\text{O}_{2n+2}$ phases are identified on the phase diagram by their formal 3d electron count. AFI, antiferromagnetic insulator; SC, superconductor. **b**, Crystal structures of the quintuple-layer nickelates in the $\text{Nd}_6\text{Ni}_5\text{O}_{16}$ Ruddlesden–Popper phase (left) and $\text{Nd}_6\text{Ni}_5\text{O}_{12}$ reduced square-planar phase (right), depicted at the same scale. Note the change in oxygen coordination upon reduction: the octahedral coordination in the five-layer structure converts to the square-planar coordination, and the rock salt layers separating every five nickel layers transform into fluorite blocking slabs. Nd, Ni and O in turquoise, red and yellow, respectively.

the ‘quintuple-layer’ compound $\text{R}_6\text{Ni}_5\text{O}_{12}$ ($n=5$) with average $d^{8.8}$ ($\text{Ni}^{1.2+}$) filling falls directly at the optimal doping to align with the cuprate phase diagram and is thus an appealing target to search for further nickelate superconductivity.

We synthesized the square-planar layered compound $\text{Nd}_6\text{Ni}_5\text{O}_{12}$ ($n=5$) with optimal nickel $d^{8.8}$ filling from its Ruddlesden–Popper parent phase $\text{Nd}_6\text{Ni}_5\text{O}_{16}$. We additionally synthesized the ‘overdoped’ layered compound $\text{Nd}_4\text{Ni}_3\text{O}_8$ ($n=3$) with $d^{8.67}$ filling, whose Ruddlesden–Popper parent phase $\text{Nd}_4\text{Ni}_3\text{O}_{10}$ has been well characterized in the bulk, to benchmark our studies^{20,21}. First, we employed reactive-oxide molecular beam epitaxy to stabilize epitaxial thin films of the oxidized Ruddlesden–Popper $\text{Nd}_{n+1}\text{Ni}_n\text{O}_{3n+1}$ compounds on (110)-orientated NdGaO_3 substrates (Methods and Supplementary Note 2). This was followed by an ex-situ CaH_2 -assisted topotactic reduction to deintercalate oxygen and convert the films into the square-planar ($\text{Nd}_{n+1}\text{Ni}_n\text{O}_{2n+2}$) phase (Methods), as has been performed in the infinite-layer compounds^{3,13}.

Cross-sectional scanning transmission electron microscopy (STEM) images of the $n=5$ parent Ruddlesden–Popper phase $\text{Nd}_6\text{Ni}_5\text{O}_{16}$ and the reduced compound $\text{Nd}_6\text{Ni}_5\text{O}_{12}$ are shown in Fig. 2a–c. Atomic-resolution high-angle annular dark-field (HAADF) and annular bright-field (ABF) images of well-ordered regions confirm both the shortening of the c axis lattice constant and the removal of apical oxygen in the neodymium planes from the $\text{Nd}_6\text{Ni}_5\text{O}_{16}$ (Fig. 2a) to the $\text{Nd}_6\text{Ni}_5\text{O}_{12}$ phase (Fig. 2b). As shown in Fig. 2c, elemental mapping by electron energy loss spectroscopy (EELS) illustrates the quintuple-layer structure with the neodymium fluorite layers of the $\text{Nd}_6\text{Ni}_5\text{O}_{12}$ film. Similar to superconducting infinite-layer nickelates^{12,13}, these samples also show regions of secondary or defect inclusions in addition to the layered nickelate phase (Supplementary Note 3 and Supplementary Figs. 4–7). The structural coherence at the bulk scale of both $n=3$ and $n=5$ Ruddlesden–Popper and square-planar phases was probed with X-ray diffraction. X-ray diffraction scans in Fig. 2d display the presence of superlattice peaks demonstrating ordering of the Ruddlesden–Popper structure. Upon reduction, we observed a

rightward shift of the superlattice peaks in the diffraction spectra, corresponding to a compression of the out-of-plane lattice constants from $c=42.5 \text{ \AA}$ to $c=38.8 \text{ \AA}$ for $\text{Nd}_6\text{Ni}_5\text{O}_{12}$, and $c=27.4 \text{ \AA}$ to $c=25.4 \text{ \AA}$ for $\text{Nd}_4\text{Ni}_3\text{O}_8$, which is consistent with the STEM imaging. Electronic characterization via EELS (Supplementary Note 3 and Supplementary Fig. 8) and X-ray absorption spectroscopy (XAS) (Supplementary Note 5 and Supplementary Fig. 11) further confirm reduction to the square-planar phase. The intense pre-peak at the O K-edge in $\text{Nd}_6\text{Ni}_5\text{O}_{16}$ associated with oxygen 2p orbitals hybridized with (formal) nickel $3d^{7+\delta}$ states is altered upon reduction²². A shoulder with weaker spectral weight emerges at higher energies in $\text{Nd}_6\text{Ni}_5\text{O}_{12}$, which is consistent with the hybridized nickel $3d^{9-\delta}$ –oxygen 2p states. This has been seen in bulk compounds^{17,18}, as well as in infinite-layer compounds that achieve similar nickel filling through chemical doping¹².

The electronic properties of the layered nickelate thin films are shown in Fig. 3. Figure 3a shows the temperature-dependent resistivities of the as-synthesized Ruddlesden–Popper compounds before reduction. The $\text{Nd}_4\text{Ni}_3\text{O}_{10}$ film exhibits a resistivity kink at $\sim 155 \text{ K}$, which is probably due to charge density wave formation^{20,21}. Our $\text{Nd}_6\text{Ni}_5\text{O}_{16}$ Ruddlesden–Popper films all display a metal-to-insulator transition with a weak hysteresis reminiscent of the first-order transition of the perovskite NdNiO_3 . Upon reduction, $\text{Nd}_4\text{Ni}_3\text{O}_8$ exhibits metallic behaviour similar to that observed in the infinite-layer NdNiO_2 (ref. ³) and trilayer $\text{Pr}_4\text{Ni}_3\text{O}_8$ (ref. ¹⁷); we note that the ground-state behaviour of bulk $\text{Nd}_4\text{Ni}_3\text{O}_8$ has not yet been well established^{21,23}. Meanwhile, $\text{Nd}_6\text{Ni}_5\text{O}_{12}$ becomes superconducting (Fig. 3b). The onset of superconductivity begins at temperatures as high as $\sim 15 \text{ K}$ with the point of maximum curvature at $\sim 13 \text{ K}$. The resistivity (ρ) reaches half the normal state value at $\sim 4.5 \text{ K}$ and hits zero ohms by $\sim 100 \text{ mK}$, as shown in the inset. The suppression of superconductivity by a magnetic field up to 9 T in the c axis perpendicular to the plane of the sample is presented in Fig. 3c (see also Supplementary Note 4 and Supplementary Fig. 9). The normal state resistivity is approximately linear with temperature immediately before approaching the superconducting transition and responds

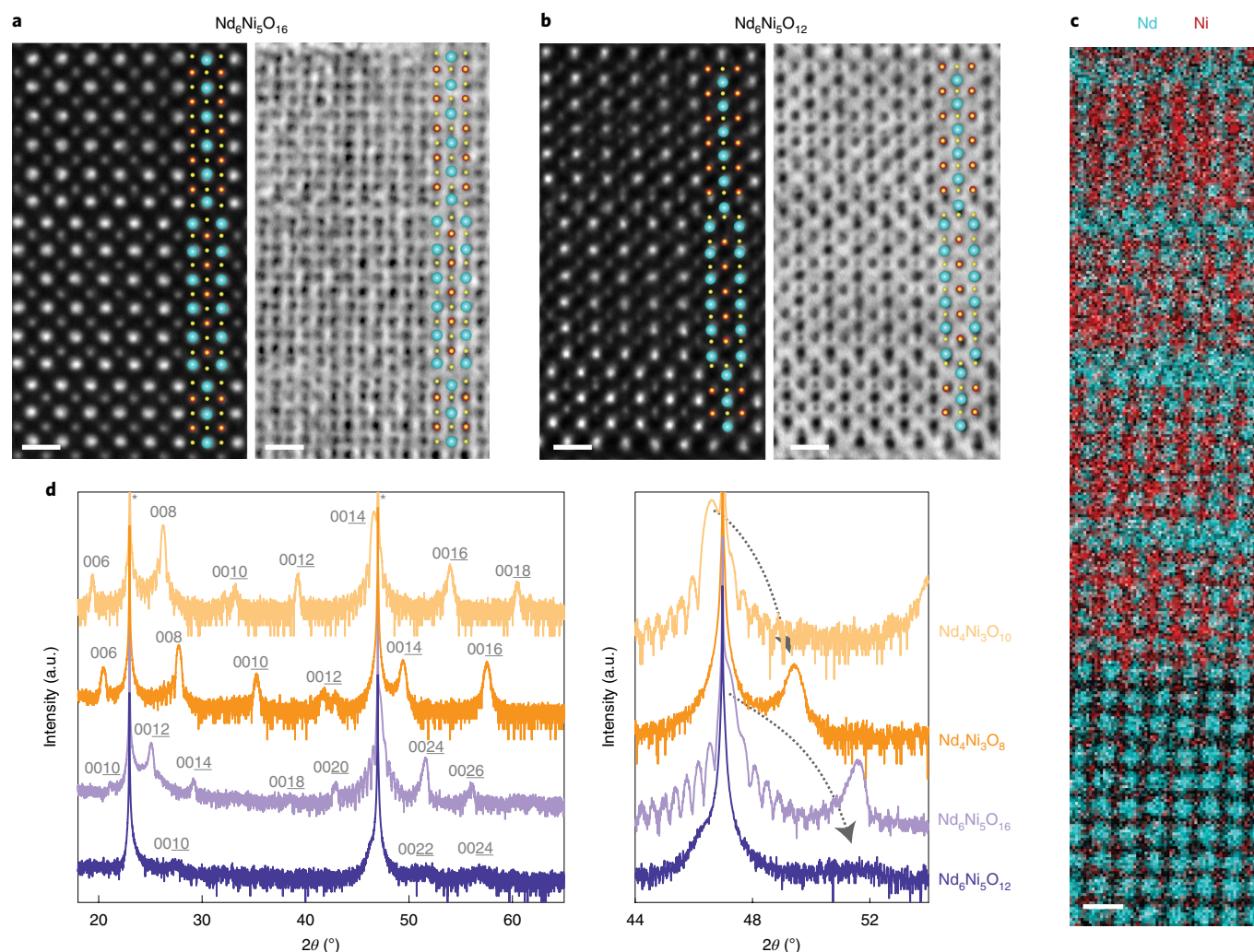


Fig. 2 | Structural characterization of the layered nickelates. **a, b**, High-angle annular dark-field (left) and annular bright-field (right) STEM images of the Nd₆Ni₅O₁₆ (**a**) and Nd₆Ni₅O₁₂ (**b**) compounds. Nd, Ni and O are represented by turquoise, red and yellow dots, respectively. Scale bars, 5 Å. **c**, EELS map of the Nd₆Ni₅O₁₂ compound near the substrate-film interface. Scale bar, 5 Å. **d**, X-ray diffraction spectra of the $n=3$ and $n=5$ compounds over the full scan range (left). Substrate peaks are labelled with asterisks and curves are vertically offset for clarity. A zoomed-in region (right) illustrates how the main superlattice peaks ((0014) for $n=3$ and (0022) for $n=5$) shift upon reduction, as indicated by the grey arrows.

minimally to an out-of-plane magnetic field. Due to the breadth of the transition, we use the strength of the field where the resistivity reaches 90% of the normal state value, where superconducting correlations are present, as a proxy for the upper critical field $H_{c, \perp}$ (ref. 24). Being linear in the Ginzburg–Landau model (inset, Fig. 3c; Methods) around T_c , this allows us to estimate an in-plane correlation length of $\xi(T=0)_{ab} = 4.4 \pm 0.2$ nm, which is comparable to that of the doped infinite-layer compound^{3,24}.

Particularly noteworthy in the context of infinite-layer nickelates is the temperature dependence of the Hall coefficient (Fig. 3d). The doped infinite-layer nickelates possess Hall coefficients that, while sensitive to factors such as doping levels^{7,8,25}, thickness²⁶ and cation composition^{25,27,28}, ultimately remain negative at all temperatures or exhibit a zero-crossing. This evinces a two-band picture with substantive electron- and hole-pocket contributions^{3,10,11}. Meanwhile, both the superconducting Nd₆Ni₅O₁₂ and non-superconducting Nd₄Ni₃O₈ layered nickelates have Hall coefficients that remain positive at all temperatures, with a semiconductor-like temperature dependence reminiscent of the underdoped and optimally doped layered cuprates²⁹. For reference, we note that the Hall coefficients

of oxidized Ruddlesden–Popper thin films behave as expected (Supplementary Fig. 10): the sudden jump in the Hall coefficient (R_H) below ~ 155 K for Nd₄Ni₃O₁₀ probably reflects a Fermi surface reconstruction due to a charge density wave instability and the abrupt loss of carriers, as has been observed in the bulk²¹.

With this observation, it becomes relevant to compare the predicted electronic structure of Nd₆Ni₅O₁₂ ($n=5$) square-planar layered nickelates with their infinite-layer NdNiO₂ ($n=\infty$) and trilayer Nd₄Ni₃O₈ ($n=3$) counterparts (see Fig. 4). In NdNiO₂ (d^9 filling), much attention has been paid to its multiband character: in the paramagnetic state, in addition to the Ni- $d_{x^2-y^2}$ bands, Nd d states also cross the Fermi level. The latter lead to the appearance of electron pockets at the Γ and A points, which display mainly Nd- d_{z^2} and Nd- d_{xy} character, respectively. These electron pockets give rise to self-doping of the large hole-like Ni- $d_{x^2-y^2}$ Fermi surface^{9,10,30}. Notably, the electronic structure is three-dimensional-like, with a large c axis dispersion. In contrast, in Nd₄Ni₃O₈ (at $d^{8.67}$ filling), a single band per nickel crosses the Fermi level and there is no Nd d involvement; this leads to a much more cuprate-like scenario³¹. The electronic structure of Nd₆Ni₅O₁₂ seems to interpolate between these

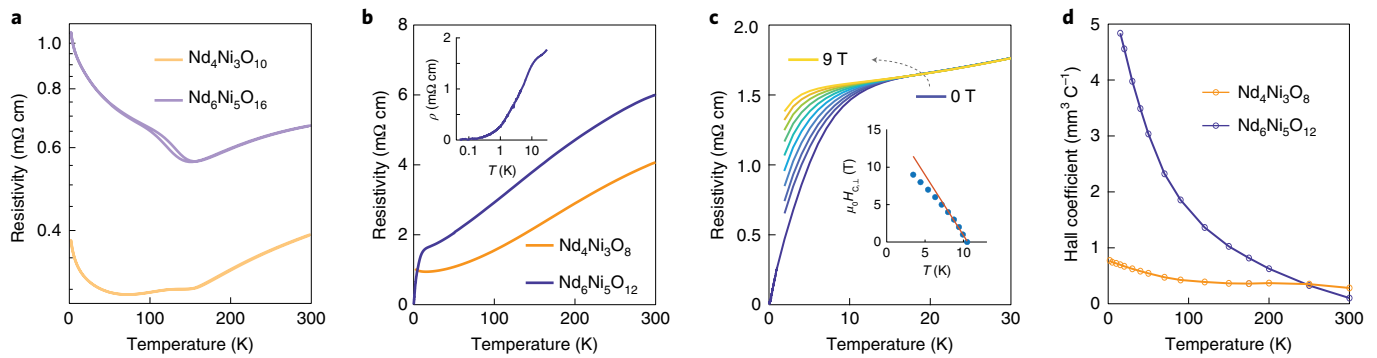


Fig. 3 | Transport properties of the layered nickelate thin films. **a**, Resistivity $\rho(T)$ for the unreduced $\text{Nd}_4\text{Ni}_3\text{O}_{10}$ ($n=3$) and $\text{Nd}_6\text{Ni}_5\text{O}_{16}$ ($n=5$) Ruddlesden-Popper compounds. **b**, Resistive transitions of the layered square-planar $\text{Nd}_4\text{Ni}_3\text{O}_8$ ($n=3$) and $\text{Nd}_6\text{Ni}_5\text{O}_{12}$ ($n=5$) compounds into the insulating upturn and superconducting states, respectively. Inset: a close-up of the superconducting transition of the $n=5$ compound from 50 mK to 30 K with temperature plotted on a log scale. **c**, Resistivity $\rho(T)$ of the $\text{Nd}_6\text{Ni}_5\text{O}_{12}$ ($n=5$) below $T=30$ K for $\mu_0 H_{c,\perp}=0-9$ T in increments of 1 T. The zero-field resistivity is reduced to 50 mK; all else is reduced to 1.8 K. Inset: the relationship between $\mu_0 H_{c,\perp}$ and T_c , with a linear scaling and fit near T_c . **d**, Temperature-dependent Hall coefficients for the reduced $\text{Nd}_4\text{Ni}_3\text{O}_8$ and $\text{Nd}_6\text{Ni}_5\text{O}_{12}$ compounds.

two situations: a single $d_{x^2-y^2}$ band per nickel crosses the Fermi level but Nd $5d$ bands start playing a role, even though the electron pockets related to Nd $5d$ states are substantially smaller than those in the infinite-layer material³². These features of the electronic structure suggest that Nd-Ni $5d-3d$ hybridization is less important in $\text{Nd}_6\text{Ni}_5\text{O}_{12}$ than in the infinite-layer compounds. Aside from the appearance of the neodymium-derived pockets at the zone corners, the Fermi surface of $\text{Nd}_6\text{Ni}_5\text{O}_{12}$ is analogous to that of multilayer cuprates with one electron-like and four hole-like $d_{x^2-y^2}$ Fermi surface sheets³³. Importantly, the Fermi surface of the quintuple-layer nickelate is much more two-dimensional-like compared to the infinite-layer nickelate compound, as the presence of the fluorite blocking layer cuts the c axis dispersion. From our description of the electronic structure, we calculated low-temperature Hall coefficients (R_H) using semi-classical Boltzmann transport theory (Supplementary Note 6). In the $T=0$ limit, we find $R_H \approx 1 \text{ mm}^3 \text{ C}^{-1}$ and $5 \text{ mm}^3 \text{ C}^{-1}$ for $\text{Nd}_4\text{Ni}_3\text{O}_8$ and $\text{Nd}_6\text{Ni}_5\text{O}_{12}$, respectively. These values are consistent with the experimental low-temperature R_H presented above and suggest that, even at identical $d^{8,8}$ filling levels, the layered $\text{Nd}_6\text{Ni}_5\text{O}_{12}$ compound has a weaker involvement of the Nd d bands and is more cuprate-like than its Sr-doped NdNiO_2 counterpart.

In the cuprates, a large $p-d$ hybridization is an essential ingredient in mediating high-temperature superconductivity³⁴. A quantitative measurement of this is the charge-transfer energy, Δ , which is inversely proportional to the hybridization. In the context of infinite-layer superconducting nickelates, the larger charge-transfer energy ($\Delta_{112} \cong 4.4 \text{ eV}$)^{10,12} compared to cuprates has been intensively analysed. From electronic structure calculations, Δ can be obtained as the difference in energy between the Ni- $d_{x^2-y^2}$ and the O- $p\sigma$ on-site energies derived from maximally localized Wannier functions (Supplementary Note 6). The charge-transfer energy for $\text{Nd}_4\text{Ni}_3\text{O}_8$ is $\Delta_{438} \cong 3.5 \text{ eV}$, consistent with previous work³⁵, and for $\text{Nd}_6\text{Ni}_5\text{O}_{12}$ $\Delta_{6512} \cong 4.0 \text{ eV}$. These are substantially smaller values than those obtained for the infinite-layer compounds. We can qualitatively assess this calculation using XAS on our synthesized films. Spectra at the O K-edge for the $\text{Nd}_6\text{Ni}_5\text{O}_{12}$ and $\text{Nd}_4\text{Ni}_3\text{O}_8$ compounds each exhibit a pre-peak feature whose intensity increase with diminishing dimensionality (Supplementary Fig. 11). Since the pre-peak corresponds to excitations from the O $1s$ states to hybridized Ni-O $2p-3d$ states, comparisons of pre-peak intensities can be used as a proxy to estimate the relative size of the charge-transfer gap or transition metal-oxygen hybridization³⁶. Meanwhile, no pre-peak has been observed in undoped infinite-layer nickelates¹¹.

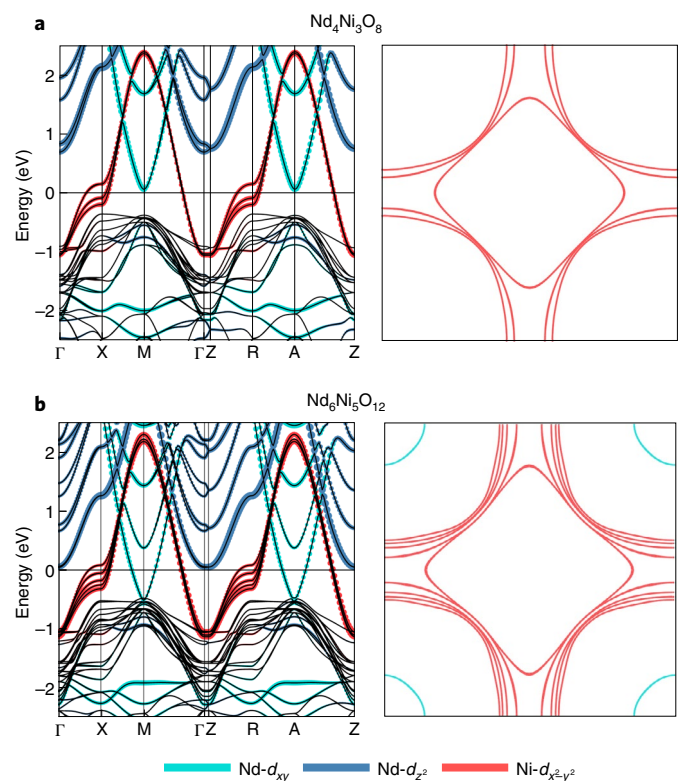


Fig. 4 | Electronic structure description of the layered nickelates.

a, b, Layered $\text{Nd}_4\text{Ni}_3\text{O}_8$ ($n=3$) (**a**) and $\text{Nd}_6\text{Ni}_5\text{O}_{12}$ ($n=5$) (**b**) paramagnetic band structures and corresponding Fermi surfaces with Nd- d_{xy} , Nd- d_{z^2} and Ni- $d_{x^2-y^2}$ orbital-site content ('fatbands') highlighted.

Hence, our calculations and XAS jointly suggest a slightly reduced charge-transfer energy and enhanced covalency in the layered nickelates compared to the infinite-layer compounds.

We have synthesized a quintuple-layer square-planar nickelate that demonstrates superconductivity with a T_c of ~ 13 K. Our square-planar trilayer and quintuple-layer compounds possess similarities to the doped infinite-layer nickelates, but notably have positive Hall coefficients up to room temperature, which is indicative of a more single-band-like picture. This, in tandem with our

theoretical description, suggests that the quintuple-layer $\text{Nd}_6\text{Ni}_5\text{O}_{12}$ compound possesses an electronic structure that is qualitatively intermediate between that of the cuprates and infinite-layer nickelates, and tunable by the dimensionality of the system. In revealing superconductivity in a new layered nickelate compound, we unlock the rare-earth nickelates as a family of superconductors beyond the doped infinite-layer compound. While the nickelates are their own class of superconductors distinct from the cuprates, it is intriguing that the cuprate-motivated predictions of optimal $d^{8.8}$ filling have yielded superconductivity, whether achieved through chemical doping or layering dimensionality. Our work opens up future avenues in which chemical doping and artificial layering may be harnessed in concert to map out and optimize superconductivity. In this vein, we suggest that exploring the phase diagram around optimal $d^{8.8}$ filling by using Sr^{2+} or Ce^{4+} to chemically dope a layered nickelate may be an exciting route to further expand the family of nickelate superconductors.

Online content

Any methods, additional references, Nature Research reporting summaries, source data, extended data, supplementary information, acknowledgements, peer review information; details of author contributions and competing interests; and statements of data and code availability are available at <https://doi.org/10.1038/s41563-021-01142-9>.

Received: 21 April 2021; Accepted: 23 September 2021;

Published online: 22 November 2021

References

- Bednorz, J. & Müller, K. Possible high T_c superconductivity in the Ba–La–Cu–O system. *Z. Phys. B* **64**, 189–193 (1986).
- Keimer, B., Kivelson, S. A., Norman, M. R., Uchida, S. & Zaanen, J. From quantum matter to high-temperature superconductivity in copper oxides. *Nature* **518**, 179–186 (2015).
- Li, D. et al. Superconductivity in an infinite-layer nickelate. *Nature* **572**, 624–627 (2019).
- Anisimov, V. I., Bukhvalov, D. & Rice, T. M. Electronic structure of possible nickelate analogs to the cuprates. *Phys. Rev. B* **59**, 7901–7906 (1999).
- Chaloupka, J. & Khaliullin, G. Orbital order and possible superconductivity in $\text{LaNiO}_3/\text{LaMO}_3$ superlattices. *Phys. Rev. Lett.* **100**, 016404 (2008).
- Emery, V. J., Kivelson, S. A. & Tranquada, J. M. Stripe phases in high-temperature superconductors. *Proc. Natl Acad. Sci. USA* **96**, 8814–8817 (1999).
- Li, D. et al. Superconducting dome in $\text{Nd}_{1-x}\text{Sr}_x\text{NiO}_2$ infinite layer films. *Phys. Rev. Lett.* **125**, 027001 (2020).
- Zeng, S. et al. Phase diagram and superconducting dome of infinite-layer $\text{Nd}_{1-x}\text{Sr}_x\text{NiO}_2$ thin films. *Phys. Rev. Lett.* **125**, 147003 (2020).
- Lee, K.-W. & Pickett, W. E. Infinite-layer LaNiO_2 : Ni^{1+} is not Cu^{2+} . *Phys. Rev. B* **70**, 165109 (2004).
- Botana, A. S. & Norman, M. R. Similarities and differences between LaNiO_2 and CaCuO_2 and implications for superconductivity. *Phys. Rev. X* **10**, 011024 (2020).
- Hepting, M. et al. Electronic structure of the parent compound of superconducting infinite-layer nickelates. *Nat. Mater.* **19**, 381–385 (2020).
- Goodge, B. H. et al. Doping evolution of the Mott–Hubbard landscape in infinite-layer nickelates. *Proc. Natl Acad. Sci. USA* **118**, e2007683118 (2021).
- Lee, K. et al. Aspects of the synthesis of thin film superconducting infinite-layer nickelates. *APL Mater.* **8**, 041107 (2020).
- Gu, Q. et al. Single particle tunneling spectrum of superconducting $\text{Nd}_{1-x}\text{Sr}_x\text{NiO}_2$ thin films. *Nat. Commun.* **11**, 6027 (2020).
- Li, Q. et al. Absence of superconductivity in bulk $\text{Nd}_{1-x}\text{Sr}_x\text{NiO}_2$. *Commun. Mater.* **1**, 16 (2020).
- Wang, B.-X. et al. Synthesis and characterization of bulk $\text{Nd}_{1-x}\text{Sr}_x\text{NiO}_2$ and $\text{Nd}_{1-x}\text{Sr}_x\text{NiO}_3$. *Phys. Rev. Mater.* **4**, 084409 (2020).
- Zhang, J. et al. Large orbital polarization in a metallic square-planar nickelate. *Nat. Phys.* **13**, 864–869 (2017).
- Lin, J. Q. et al. Strong superexchange in a $d^{9-\delta}$ nickelate revealed by resonant inelastic X-ray scattering. *Phys. Rev. Lett.* **126**, 087001 (2021).
- Mukuda, H., Shimizu, S., Iyo, A. & Kitaoka, Y. High- T_c superconductivity and antiferromagnetism in multilayered copper oxides—a new paradigm of superconducting mechanism. *J. Phys. Soc. Jpn* **81**, 011008 (2012).
- Greenblatt, M. Ruddlesden–Popper $\text{Ln}_{n+1}\text{Ni}_n\text{O}_{3n+1}$ nickelates: structure and properties. *Curr. Opin. Solid State Mater. Sci.* **2**, 174–183 (1997).
- Li, Q. et al. Contrasting physical properties of the trilayer nickelates $\text{Nd}_4\text{Ni}_3\text{O}_{10}$ and $\text{Nd}_4\text{Ni}_3\text{O}_8$. *Sci. China Phys. Mech. Astron.* **64**, 227411 (2020).
- Abbate, M. et al. Electronic structure and metal-insulator transition in $\text{LaNiO}_{3-\delta}$. *Phys. Rev. B* **65**, 155101 (2002).
- Miyatake, T. et al. Chemical substitution effect of high- T_c superconductor candidate $\text{R}_2\text{Ni}_2\text{O}_8$ (R: rare-earth). *JPS Conf. Proc.* **30**, 011061 (2020).
- Wang, B. Y. et al. Isotropic Pauli-limited superconductivity in the infinite-layer nickelate $\text{Nd}_{0.775}\text{Sr}_{0.225}\text{NiO}_2$. *Nat. Phys.* **17**, 473–477 (2021).
- Osada, M. et al. A superconducting praseodymium nickelate with infinite layer structure. *Nano Lett.* **20**, 5735–5740 (2020).
- Zeng, S. et al. Observation of perfect diamagnetism and interfacial effect on the electronic structures in $\text{Nd}_{0.8}\text{Sr}_{0.2}\text{NiO}_2$ superconducting infinite layers. Preprint at <https://arxiv.org/abs/2104.14195> (2021).
- Osada, M. et al. Nickelate superconductivity without rare-earth magnetism: $(\text{La}, \text{Sr})\text{NiO}_2$. *Adv. Mater.* <https://doi.org/10.1002/adma.202104083> (2021).
- Zeng, S. et al. Superconductivity in infinite-layer lanthanide nickelates. Preprint at <https://arxiv.org/abs/2105.13492> (2021).
- Takagi, H. et al. Superconductor-to-nonsuperconductor transition in $(\text{La}_{1-x}\text{Sr}_x)_2\text{CuO}_4$ as investigated by transport and magnetic measurements. *Phys. Rev. B* **40**, 2254 (1989).
- Wu, X. et al. Robust $d_{x^2-y^2}$ -wave superconductivity of infinite-layer nickelates. *Phys. Rev. B* **101**, 060504(R) (2020).
- Karp, J. et al. Comparative many-body study of $\text{Pr}_2\text{Ni}_2\text{O}_8$ and NdNiO_2 . *Phys. Rev. B* **102**, 245130 (2020).
- LaBollita, H. & Botana, A. S. Electronic structure and magnetic properties of higher-order layered nickelates: $\text{La}_{n+1}\text{Ni}_n\text{O}_{2n+2}$ ($n=4-6$). *Phys. Rev. B* **104**, 035148 (2021).
- Sakakibara, H. et al. Orbital mixture effect on the Fermi-surface– T_c correlation in the cuprate superconductors: bilayer vs. single layer. *Phys. Rev. B* **89**, 224505 (2014).
- Zhang, F. C. & Rice, T. M. Effective Hamiltonian for the superconducting Cu oxides. *Phys. Rev. B* **37**, 3759(R) (1988).
- Nica, E. M. et al. Theoretical investigation of superconductivity in trilayer square-planar nickelates. *Phys. Rev. B* **102**, 020504(R) (2020).
- Suntivich, J. et al. Estimating hybridization of transition metal and oxygen states in perovskites from O K-edge X-ray absorption spectroscopy. *J. Phys. Chem. C* **118**, 1856–1863 (2014).

Publisher's note Springer Nature remains neutral with regard to jurisdictional claims in published maps and institutional affiliations.

© The Author(s), under exclusive licence to Springer Nature Limited 2021

Methods

Synthesis of layered nickelate thin films. The elemental fluxes from the effusion cells were first estimated by synthesizing thin films of NiO on MgO and Nd₂O₃ on yttria-stabilized zirconia. The thickness of these films was extracted from X-ray reflectivity fits. These deposition rates were also verified using Rutherford backscattering spectrometry. Using these flux estimates, we then synthesized NdNiO₃ on LaAlO₃ to refine the stoichiometry³⁷. X-ray reflectivity fits of the optimized NdNiO₃ films were used to determine the overall monolayer dosage. Using these optimized conditions, all layered Ruddlesden–Popper nickelate films were then synthesized by sequentially depositing the neodymium and nickel sources using shutter times found from NdNiO₃, starting with neodymium at the interface. Reflection high-energy electron diffraction was used in situ to monitor the formation of secondary phases and adjust the substrate temperature and/or shutter times of the neodymium and nickel sources accordingly. Distilled ozone flow (Heeg Vacuum Engineering) was controlled with a piezoelectric leak valve to maintain total chamber pressures in excess of 1.5×10^{-6} Torr to ensure the full oxidation of nickel into the 2.67+ or 2.8+ states for the Nd₄Ni₃O₁₀ and Nd₆Ni₅O₁₆ compounds, respectively. Films were synthesized to contain a total of 60 Ni–O layers, ~27 nm for Nd₄Ni₃O₁₀ and ~25 nm for Nd₆Ni₅O₁₆. All films were cooled in 1×10^{-6} Torr of distilled ozone to discourage the formation of oxygen vacancies. None of the films were deposited with capping layers as has been performed elsewhere^{3,13,37}. We note that the successful synthesis of the Nd₄Ni₃O₁₀ yielding superconducting films is the most sensitive aspect of this experiment, and provide additional details in Supplementary Note 2.

The oxidized Ruddlesden–Popper films were then reduced into the layered square-planar phase using topotactic CaH₂ methods similar to those described elsewhere^{3,13}. The as-synthesized films were cut into $\sim 2.5 \times 5$ mm² pieces; gently wrapped in aluminium foil suitable for ultra-high vacuum (All-Foils) and inserted into borosilicate tubes (Chemglass Life Sciences), pre-baked at 200 °C, with ~100 mg of CaH₂ pellets (>92%, Alfa Aesar). The glass tubes were sealed while being pumped with a small turbomolecular pump down to <0.5 mTorr. Reductions were conducted in a convection oven (Heratherm, Thermo Fisher Scientific) at 260–300 °C for 3–6 hours, with heating rates of 10 °C min⁻¹. After reduction, the films were briefly sonicated in 2-butanone and isopropanol to remove CaH₂ residue. Additional details on the synthesis can be found in Supplementary Note 2.

Structural characterization. X-ray diffraction was performed with a Malvern Panalytical Empyrean diffractometer using Cu K α 1 radiation. Reciprocal space maps (Supplementary Fig. 3) were taken using a two-dimensional pixel detector (PIXcel3D). Cross-sectional TEM specimens were prepared using a Thermo Fisher Scientific Helios G4 UX and/or an FEI Helios 660 focused ion beam (FIB) with a final thinning step at 2 keV. HAADF- and ABF-STEM was performed using an aberration-corrected Thermo Fisher Scientific Spectra 300 X-FEG operated at 300 kV with a probe convergence semi-angle of 30 mrad. EELS measurements were carried out at 120 kV on the same instrument equipped with a Gatan Continuum spectrometer and camera. Any cleaning procedures of the FIB lamellas involving oxygen plasma were foregone for the reduced square-planar samples to prevent reoxidation into the Ruddlesden–Popper phase. Additional details may be found in Supplementary Note 3.

Transport measurements. Devices in Hall bar geometries were patterned using typical UV photolithography processes. Designs were written on 4-inch fused silica mask plates using a Heidelberg DWL-2000 mask maker with a 4-mm write head. The photolithography for the ion milling and deposition patterns was done using a conventional SPR 220-based process. All samples were ion-milled using an Intivac Nanoquest II Ar ion mill at a working temperature of 15 °C (to prevent sample reoxidation) and an incident beam angle of 10°. The Ti(10)/Pt(100) (units in nm) metal contact layer was deposited on top of a deposition lithography mask via pulsed laser deposition for a standard metal lift-off process. In some cases, Cr(5)/Au(100) (units in nm) metal contact layers were deposited with an electron-beam evaporator and Hall bar channels defined by a diamond scribe. Transport measurements down to 1.8 K were conducted in a Quantum Design Physical Property Measurement System equipped with a 9-T magnet using standard a.c. lock-in techniques at ~15 Hz. Below 1.8 K, measurements were performed in a Leiden Cryogenics CF-700 dilution refrigerator down to ~50 mK. To avoid capacitive losses from high excitation a.c. frequencies which are exacerbated at low temperatures, resistances below 1.8 K were extracted from current–voltage (*I*–*V*) sweeps performed using d.c. techniques. A total of 4–5 *I*–*V* sweeps at each point were averaged to improve the d.c. signal-to-noise and resistances were taken from the slope fitted across ± 0.5 μ A. Hall coefficients were calculated using field sweeps up to 9 T; a representative example is shown in Supplementary Fig. 10.

XAS. XAS was performed at 78 K in the total electron yield at Beamlines 4.0.2 and 6.3.1 at the Advanced Light Source at Lawrence Berkeley National Laboratory. All spectra presented are polarization averaged and normalized to the signal impinging on a copper mesh. The spectra are further scaled at the pre-edge and normalized across the entire edge to compare relative intensities. Each spectrum presented in Supplementary Fig. 11 represents the average of 8–12 individual scans.

Computational methods. To calculate the paramagnetic electronic structure of the *n* = 3 and *n* = 5 layered nickelates, we employed density functional theory calculations using the projector augmented wave method, as implemented in the Vienna ab initio simulation package³⁸. We used a pseudopotential that treats the Nd 4*f* electrons as core electrons. The in-plane lattice parameters were set to match the NdGaO₃ substrate, and the out-of-plane lattice parameter was optimized. We find that our optimizations agree well with the experimentally measured lattice parameters (see Supplementary Note 6 for more details as well as for the calculations of the Hall coefficient).

To study the dominant pairing instability for the *n* = 5 compound, we solved an effective *t*–*J* model for the five NiO₂ layers using a slave-boson representation and generalizing the spin symmetry of the model to Sp(*N*) for large *N* to obtain the superconducting gap order parameter as a function of filling. We decoupled the exchange interactions in both Hartree and pairing channels, and obtained saddle-point solutions as functions of the total nickel doping. A detailed description of the *t*–*J* model and its corresponding solutions is presented in Supplementary Note 7.

Data availability

The data supporting the findings of this study are available from the corresponding authors upon reasonable request. Source data for Figs. 2–4 are provided with this paper.

References

- Li, Y. et al. Impact of cation stoichiometry on the crystalline structure and superconductivity in nickelates. *Front. Phys.* **9**, 719534 (2021).
- Kresse, G. & Furthmüller, J. Efficient iterative schemes for ab initio total-energy calculations using a plane-wave basis set. *Phys. Rev. B* **54**, 11169 (1996).

Acknowledgements

We thank M. R. Norman and M. Mitrano for discussions. We also thank K. Lee and H. Y. Hwang for discussions and technical guidance in reduction experiments; D. Erdosy, J. Lee, N. Pappas, S. Thapa and M. Wenny for continued support in reductions; H. Hijazi at the Rutgers University Laboratory of Surface Modification for assistance in Rutherford backscattering spectrometry; and J. MacArthur for electronics support. This research was funded in part by the Gordon and Betty Moore Foundation's EPIQS Initiative, grant no. GBMF6760 to J. A. Mundy. Materials growth and electron microscopy were supported in part by the Platform for the Accelerated Realization, Analysis, and Discovery of Interface Materials (PARADIM) under NSF Cooperative Agreement no. DMR-2039380. Electron microscopy made use of the Cornell Center for Materials Research (CCMR) Shared Facilities, which are supported through the NSF MRSEC Program (no. DMR-1719875). The Thermo Fisher Spectra 300 X-CFEG was acquired with support from PARADIM, an NSF MIP (DMR-2039380) and Cornell University. Nanofabrication work was performed in part at Harvard University's Center for Nanoscale Systems (CNS), a member of the National Nanotechnology Coordinated Infrastructure Network (NNCI), supported by the National Science Foundation under NSF grant no. 1541959, and in part at the University of Michigan Lurie Nanofabrication Facility. This research used resources of the Advanced Light Source, a US DOE Office of Science User Facility under contract no. DE-AC02-05CH11231. G.A.P. acknowledges support from the Paul & Daisy Soros Fellowship for New Americans and from the NSF Graduate Research Fellowship grant no. DGE-1745303. G.A.P. and D.E.S. acknowledge support from US Department of Energy, Office of Basic Energy Sciences, Division of Materials Sciences and Engineering, under award no. DE-SC0021925. Q.S., S.D. and D.C.C. were supported by the STC Center for Integrated Quantum Materials, NSF grant no. DMR-1231319. B.H.G., H.P. and L.F.K. acknowledge support by PARADIM, NSF no. DMR-2039380. A.T.P. acknowledges support from the Department of Defense through the National Defense Science and Engineering Graduate Fellowship (NDSEG) Program. J. A. Mason acknowledges support from the Arnold and Mabel Beckman Foundation through a Beckman Young Investigator grant. O.E. acknowledges support from NSF grant no. DMR-1904716. A.S.B. and H.L. acknowledge NSF grant no. DMR-2045826 and the ASU Research Computing Center for HPC resources. J. A. Mundy acknowledges support from the Packard Foundation.

Author contributions

G.A.P., Q.S., C.M.B. and J. A. Mundy synthesized the thin films with assistance from H.P. G.A.P., D.E.S. and S.D. conducted the reductions with guidance from J. A. Mason. B.H.G. and L.F.K. characterized the samples with scanning transmission electron microscopy. G.A.P., A.T.P. and A.Y. performed transport measurements using fabrication assistance from S.N. and J.T.H. G.A.P., D.E.S., Q.S., D.C.C., A.T.N. and P.S. performed X-ray absorption spectroscopy. H.L. and A.S.B. performed density functional theory calculations. E.M.N., O.E. and A.S.B. constructed the *t*–*J* model. A.S.B. and J. A. Mundy conceived and guided the study. G.A.P., A.S.B. and J. A. Mundy wrote the manuscript with discussion and contributions from all authors.

Competing interests

The authors declare no competing interests.

Additional information

Supplementary information The online version contains supplementary material available at <https://doi.org/10.1038/s41563-021-01142-9>.

Correspondence and requests for materials should be addressed to Antia S. Botana or Julia A. Mundy.

Peer review information *Nature Materials* thanks Hai-Hu Wen and the other, anonymous, reviewer(s) for their contribution to the peer review of this work.

Reprints and permissions information is available at www.nature.com/reprints.